Volume 1 | Number 1 | Jan 2013 | Pages 1–100

Green Chemistry

Cutting-edge research for a greener sustainable future

www.rsc.org/greenchem

Stille couplings in water @RT

ROYAL SOCIETY OF CHEMISTRY

ROYAL SOCIETY OF CHEMISTRY

www.rsc.org/greenchem

SCHOLARONE™
Manuscripts

Journal Name

ARTICLE

One pot synthesis of environmentally friendly lignin nanoparticles with compressed liquid carbon dioxide as an antisolvent†

Aye Aye Myint,[a] Hun Wook Lee,[a] Bumjoon Seo,[a] Won-Su Son,[a] Junho Yoon,[a] Tae Jun Yoon,[a] Hee Jeong Park,[a] Jihyun Yu,[a,b] Jeyong Yoon[a,b] and Youn-Woo Lee*[a]

Nanoparticles from the commercial kraft lignin were developed using a facile, one pot green technology of compressed CO_2 antisolvent. *N,N,*-dimethylformamide (DMF) was employed as an organic solvent to prepare the lignin solution. The effects of various process parameters: temperature, pressure, solution flow rate and initial solution concentration, on the product yields, morphology, size, size distribution, surface area and textural properties of the particles were investigated by FESEM, HRTEM and BET analyzers, and their formation mechanisms were deduced by the solubility behaviors of lignin with liquid CO_2 and DMF in the operating system. Moreover, the quality of the lignin nanoparticles were elucidated by ATR-FTIR, XPS, XRD, DSC, TG/DTA and UV-vis measurements. This study showed that as the temperature and lignin concentration increased, and pressure and solution flow rate decreased, the degree of particle aggregation/coalescence and size increased along with the broader in size distribution. In particular, the coalescence of particles was strongly influenced by the operation pressure, and even more significant with the temperature increased. As a result, a uniform, quasi-spherical nanoparticles with mean particle diameter of 38 nm were obtained at 280.2 K, 15.0 MPa, 0.06 kg/h of solution flow rate and 5.3 wt% of initial lignin concentration. Besides, the lignin nanoparticles have relatively higher BET surface area (nearly 92 m^2/g) which primarily consisted of mesopores, and exhibited higher UV absorbing and dispersion stability, enhanced solubility, homogeneous thermal degradation activity as compared with the raw lignin. Noteworthy, its biodegradable and biocompatible character may find it a candidate for applications in cosmetics, health and drug delivery systems.

Introduction

As the recent advances in material science and nano-engineering in the last decade, polymer nanoparticles have become very attractive for their applications in the fields of biomedicine and human health care for a broad range of product.[1-3] On the other hand, the incentive from the shortage of fossil sources and sustainable development is motivating extensive research on the development of "green processes" or new and alternative polymer nanoparticles from renewable resources.[4–5] The use of polymers from natural resources have

been shown many benefits for novel polymeric nanoparticle systems since such polymers have a variety of beneficial properties such as biodegradability and biocompatibility, they are readily available on large scale and at low cost.[6]

Lignin, one of the most abundant renewable aromatic biopolymers, is extracted from plants and represents approximately 15–30% of their total biomass besides cellulose as the major component.[7] Lignin is a highly branched polyphenolic, three-dimensional amorphous macromolecular polymer and is readily available as an industrial waste product of pulp and biofuel productions.[8] This makes it as an attractive inexpensive, environmentally friendly and renewable alternative feedstock for the development of new green materials and chemicals. However, most of the lignin from industrial streams is relegated to low values of combustion for the production of electricity and/or heat. Currently, only 2% of lignin (mainly lignosulfonates) are applied in agricultural uses or other industries as binders, *e.g.*, for animal feed pellets, bricks, ceramics or road dust, dispersants for oil well drilling products, *etc.*[7,9] A possible reason for limiting its utilization is

[a.] School of Chemical and Biological Engineering, College of Engineering and Institute of Chemical Processes (ICP), Seoul National University, 1 Gwanak-ro, Gwanak-gu, 151–744 Seoul, Republic of Korea. E-mail: ywlee@snu.ac.kr; Tel: +82-2880-1883
[b.] World Class University (WCU) Program of Chemical Convergence for Energy & Environment (C2E2), Asian Institute for Energy, Environment & Sustainability (AIEES), Seoul National University, 1 Gwanak-ro, Gwanak-gu, 151–742 Seoul, Republic of Korea.

probably the very limited solubility of the native material and the complexity of the lignin structure with very broad molecular weight distributions and a random microstructure. On the controversy, the abundant highly functional and carriers both phenolic and aliphatic hydroxyl groups in lignin make it susceptible for chemical modification or polymerization as well as suggest the possible potential prime role as a new chemical feedstock for the development of high value materials including polyurethanes,[10,11] carbon fibers,[12,13] hydrogels[14] and biomedical products.[15–17]

Recently, the preparation of nanoparticles from lignin has gained interest given its benign nature, as an alternative to toxic nanoparticles,[18] for drug delivery system,[19] for delivery of hydrophobic molecules,[20] for enhancing UV barrier, antibacterial[21] and antioxidant properties.[22] Lignin nanoparticles can be engineered by acid and solvent-antisolvent precipitation as well as emulsification.[18] Ultrasound driven assembly or self-assembly after chemical modification of lignin can also yield micro- or nano-structural particles.[19-21] But, it is worth noting that these commonly used methods may give rise to some drawbacks, including additional separation processes for achieving dry particles, high residual organic solvent and control of particle size and size distribution, which is not so applicable in industry. In addition, nanostructural materials are materials with sizes in the $1-100$ nm range, which demonstrate unique properties and functions due to their "size effect".[23] Control size and morphology of the nanomaterials is of prime necessary in their applications, which determine the application potentials of the nanoparticles, as their properties vary significantly with size.[24] For instance, the characteristics features of lignin particles with dimensions below 100 nm are an interesting and important fields of studies in wide domains, such as: (a) in medicine to provide drugs; (b) new smart nano-sized coatings beginning to be used on an industrial scale, and also information technology (IT); (c) cars, cosmetics, chemicals and packing industries and (d) additives for plastic material industry. The obtaining of nanoparticles based on natural polymer constitutes a major concern for many research communities because of their accessibility and their environmental compatibility.[25] Therefore, developing less energy consuming, more environmentally friendly, and highly efficient methods for the synthesis of lignin nanoparticles is highly desirable and in great need.

Over the previous two decades, considerable attention has been paid to the use of "compressed/supercritical fluids" based technology as an emerging "green" technology for the formation of a wide variety of polymeric nanoparticles of control morphologies, sizes and size distributions, which is an essential necessary for their pharmaceutical and drug delivery applications.[26] As a compressed fluid, CO_2 is of particular interest in pharmaceutical processing[27–29] because of its tunable physicochemical properties near its critical conditions (T_c = 304.3 K and P_c = 7.4 MPa),[30] abundance, nonflammability, nontoxicity, inexpensiveness and environmental benignity; it is miscible with a variety of organic solvents and is readily recovered after processing. Furthermore, due to its low

polarizability per unit volume and low cohesive energy, CO_2 is a poor solvent for many macromolecules such as polymers and proteins, different antisolvent methods[31-33] have been emerging based on similar principle as liquid antisolvent precipitation.

The particle formation by compressed fluid antisolvent (PCA) technique, is a semicontinuous process, has great versatility as the properties of liquid solvents or the solute molecules can be tuned *in situ* by simply controlling the pressure and temperature of CO_2 in a single stage, and is a capable of scalable process.[34] A particular advantage of using PCA process is the organic solvent-free particles with narrow size distribution can be formed with no need of further purification and solvent removal.[35–37] In the PCA process, the polymer solution is sprayed through an atomization co-axial nozzle into the CO_2 fluid. The dissolution of the CO_2 fluid into the liquid droplet is accompanied by a large volume expansion and a reduction in the liquid solvent power. This causes a sharp rise in the supersaturation of the polymer molecules within the liquid mixture, and the formation of small, solid polymer particles.[31,38–40] As is known from previous reports,[34,35,38–42] the PCA process allows to tune particle morphology, size and distribution by manipulating various process parameters including temperature, pressure, solution injection rate, initial solute concentration of the solution and so on. However, the PCA process is very complex since it involves the coupling of thermodynamics, hydrodynamics, mass and heat transfer, and precipitation kinetics, making it difficult to elucidate the underlying mechanisms that control particle size and size distribution during PCA processing. Because of that, the position of the mixture critical point (MCP) has been introduced as a crucial parameter due to different peculiarities, such as theoretical surface tension vanishing, what effects the mass transfer and the atomization process of the technique.[29] The position of the operating region with respect to the MCP of the system CO_2-solvent is considered to be a very important in the PCA process.[41] In this context, the MCP can be defined as the pressure and temperature conditions at which the liquid-vapor mixture merges in one single compressed liquid or supercritical phase. Above the critical pressure of the MCP, the CO_2 and solvent are miscible in all the composition range and formation of solution droplets is not expected due to the inexistence of interfacial tension between the two fluids.[43,44] At these conditions mass transfer take place by turbulent mixing.[45] However, under the MCP there is droplet formation as a result of atomization by the nozzle and mass transfer takes place by molecular diffusion through the solution droplet-antisolvent interface.[41,46] Therefore, the precipitation mechanism, particle size and morphology are different above or under the MCP. Several works try to elucidate how the position of the experimental conditions with respect to the MCP can influence the particle size distribution and morphology. However, different results were observed. The best particle size has been obtained close to the MCP,[47] far above the MCP[48] and under the MCP.[49] There has also been cases in which the precipitation was not successful under the MCP due to the

existence of a liquid phase.[50] Yet, a lot of works have been reported on the precipitation of nanoparticles from numerous types of biodegradable polymers[40,42,51] but lignin has not been explored using compressed liquid CO_2 (clCO_2) as an antisolvent. Only one has reported[22] that the preparation of nanoscale lignin by supercritical antisolvent (SAS) process under one specified conditions to improve its solubility and antioxidant activity as compared with non-nanoscale lignin from organosolv process.

The main objective of this study was to design lignin nanoparticles with clCO_2 as an antisolvent by using PCA technology. To prepare nanoparticles, we focused on commercially available kraft lignin. This is a lignin residue from the kraft pulping process. It constitutes about 85% of total world lignin production.[52] Distinct from native lignin and other technical lignins, it contains a higher amount of phenolic and a lower content in aliphatic OH groups, a higher molecular weight, and a distinct solubility in alikaline solution.[53] *N,N*-dimethylformamide (DMF), is a dipolar aprotic and unassociated solvent, was used as a solvent for preparation of kraft lignin solution. Due to it is miscible with almost all common polar and nonpolar solvents, it has been used in material processing in supercritical fluid media, in the synthesis of pharmaceuticals, in agricultural chemistry, and as a solvent for polymers.[54] The influence of various process parameters on the product yields, particles' morphology, size, size distribution, surface area and textural features were investigated. To better understanding the influence of designed process parameters on the nanoparticle formation phenomena, solubility behaviors of lignin with liquid CO_2 and DMF, and the mutual solubility between liquid CO_2 and DMF under the operating conditions were deduced from their Hansen solubility parameters (HSPs). Furthermore, the quality of lignin nanoparticles were elucidated by characterizing their chemical structures, crystalline state, thermal behavior and some physical properties such as *in vitro* dissolution rate, dispersion stability and UV absorption at various pH values. Eventually, the biocompatibility and biodegradability of the lignin nanoparticles obtained at the best conditions were examined with a gram negative bacteria tagged with green fluorescence protein (*Pseudomonas aeruginosa* GFP, namely PAO1 GFP) to find their potential applications as drug delivery vehicles, in cosmetics and pharmaceuticals.

Results and discussion

The antisolvent process is based on the solute (polymer) precipitation occurring when CO_2 fluid and an organic liquid phase that contains the solute come into contact.[55,56] The interdiffusion of the organic solvent and CO_2 fluid creates conditions of solute supersaturation in the organic phase, since the newly formed CO_2-solvent mixture exhibits lower solubilization ability than that of the pure solvent. For the PCA process to be successful, CO_2 must be completely miscible with the solution solvent and the solute must also be insoluble in the CO_2 at the operating conditions. The knowledge of the

antisolvent effect of CO_2 on the solute (lignin) and the mutual solubility behavior of solvent (DMF) and CO_2 in the system is of, therefore, paramount importance.

Solubility behaviors of lignin, DMF and CO_2 in the system

In order to identify the antisolvent effect of CO_2 on lignin in the mixture CO_2-DMF system, the solubility behavior of lignin with CO_2 and DMF were quantitatively calculated by their respective HSPs at the designed experimental temperatures (280.2−298.2 K) and pressures (7.5 MPa and 15.0 MPa). The relative energy differences (RED) of DMF and CO_2 for lignin, which is depicted in Fig. 1 with the detail calculated data presented in Table S1†, were approximately 0.70−0.73 and 1.6−2.1, respectively. RED numbers less than 1.0 indicate high affinity or solubility; RED equal to or close to 1.0 is a boundary conditions; and progressively higher RED numbers indicate progressively lower affinities.[57] It is clearly indicated that liquid CO_2 acts as an antisolvent for lignin throughout the studies conditions and the level of its antisolvent ability was varied accordingly with the different temperatures and pressures. Nevertheless, the designed range of temperature and pressure is a favorable region for precipitation of lignin from the solution. We also observed only single liquid phase in the system and no droplet formation at the exit of nozzle by viewing the windowed cell during the operations. As the reference data, for the critical pressure and temperature of the binary CO_2-DMF mixture at the operating conditions (x_{CO2} = 0.81) are estimated to be approximately 5.7 MPa and 298.2 K.[58] Hence, the results of solubility studies and our observation agree with the literature data due to the working conditions are always above the critical pressure of the CO_2-DMF mixture at certain temperature.
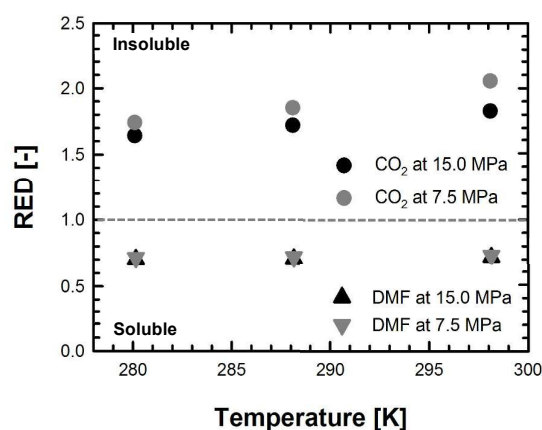

Fig. 1 The relative energy differences (RED) of DMF and CO_2 for lignin with respect to the different operational temperatures and pressures.

Moreover, it is worthwhile to note that the HSP distances (R_a) for dissolving between DMF and CO_2 each other are quite different depending on the experimental temperatures and

pressures, reported in Table S2†, indicating the mutual solubility between CO_2 and DMF is substantially influenced by varying temperatures and pressures. Whilst the solubility greatly increases with pressure, the trend as function of temperature depends on the level of pressure. Known as the retrograde behavior, the solubility decreases with increasing temperature at low pressure and increases at high pressure, the switching pressure corresponding to the crossover pressure.[55] It highlights that the degrees of solubility and location of the operating regime in the system (*i.e.*, a compressed liquid environment in this case) depending on operating conditions can potentially govern the properties of particle formed and the formation of particle phenomena during the PCA process.

Lignin precipitation performance using clCO$_2$ as an antisolvent

In order to explore the influence of process parameters on the characteristics of particle formed in the clCO$_2$ antisolvent using the PCA process, experiments were designed varying operating parameters such as temperature, pressure, solution flow rate and initial lignin concentration in the solution during DMF as an organic solvent. In all experiments, the CO_2 flow rate was maintained at 3.0 kg/h and the molar fractions of CO_2 in the CO_2-DMF mixtures during the precipitation varied from 0.90 to 0.99. In Table 1, a summary of all the experiments performed was reported, with the indication of the mean diameters with standard deviations of the particles obtained and the precipitated yields achieved.

Processed lignin yields. In all the designed experiments, particles of lignin were successfully obtained for the first study with clCO$_2$ as an antisolvent. The highest precipitation yield (nearly 90%) was achieved for the experiment performed at high initial lignin concentration of the sprayed solution under the same other conditions, PKL-8 shown in Table 1, suggesting that it substantially depends on the saturation concentration of the solute in the liquid phase formed in the precipitator. From the point of view of powders recovered in the precipitator, particles are easy to be collected, since they are released from the colloidal suspension formed in the precipitator as a fluffy powder substantially free of electrostatic charges.[59] Fig. S1† reveals the digital photographs of PKL-8 compared with that of the raw lignin (KL-raw). It is obvious that the lignin particles processed by PCA process were pale yellow color of relatively light weight fine powder whereas the raw lignin were dark brown color with a considerable heavy big particles. The lower precipitation yields were observed for the particles resulted at high temperature, low pressure and slow solution flow rate, ranging of 51−70%. This lower is likely due to the large amount of lignin might be still soluble in the DMF-CO$_2$ mixtures and existed the precipitation vessel during the experiments as like in any precipitation processes.[29,42,60] It can be explained by the consideration of the solubility behavior of the components in the system under the working conditions. As is illustrated in

Table S2†, with increasing temperature or decreasing pressure R_a values for DMF and CO_2 sequentially increased, that means the solvating power of DMF on the lignin didn't completely induce by the clCO$_2$ at the high temperature and low pressure. In the case of slow solution flow rate, the lower yield achieved is probably owing to the decrease in mixing and mass transfer rate and then this lead to lower the level of solution saturation, and thereby still remained dissolving lignin in the DMF-CO$_2$ mixture under the studied conditions.

Morphology, size and size distribution. In order to elucidate the effect of different process parameters on the morphology, particle size and size distribution of the lignin particles processed by the PCA process, the morphological characterization for the processed samples were conducted with a FESEM, and their mean particle diameters and size distributions were obtained from the particles on the FESEM images using an Image analysis software, as mentioned in the experimental method. To provide comparison with the processed lignin samples, unprocessed/raw lignin was analyzed as received using a FESEM. As can be seen in Fig. 2(a-h) and Table 1, the lignin particles obtained under all conditions are more or less aggregated/coalesced quasi-spherical nanosized particles with a maximum mean diameter of smaller than 80 nm, depending on the process parameters. In contrast, the raw lignin, KL-raw in Fig. 2(i), is constituted of irregular spherical shape of microparticles with a wide range of sizes between 29.7 and 69.9 μm measured by a wet particle analyzer.

For investigating the effect of temperature on particle morphology, size and size distribution, experiments were performed at various temperatures: from 280.2 K to 298.2 K. In all cases, the pressures were kept at 15.0 or 7.5 MPa, solution flow rate was 0.06 kg/h and initial lignin concentration was 5.3 wt%. It is apparent that the morphology, size and distribution of the processed nanoparticles were significantly influenced by temperature with respect to pressure under the studied conditions. At the same pressure, as the temperature increased the particle mean diameter and degree of aggregation/coalescence increased and particle size distribution was also broader, see Fig. 2(a-h), Fig. 2(j) and Table 1. Particularly, the morphologies of nanoparticles were very different depending on the pressure. For instance, the nanoparticles formed at low pressure of 7.5 MPa were much more aggregated and coalesced (fused) than those produced at high pressure of 15.0 MPa at the same temperature, suggesting a clear effect of pressure on the coalescence of nanoparticles and it is important to select the operating pressure; which should be far above the pressure of MCP of the CO$_2$-DMF system, to prevent this pressure effect on particle coalescence. At 7.5 MPa, primary particles are roughly spherical, but they are almost indistinguishable since most of them look as if they were melted together, which is consistent with the results obtained from previous reports using SAS

Table 1 Effects of temperature (T), pressure (P), initial lignin concentration (C_{lign}), lignin solution flow rate ($F_{sol'n}$), CO_2 density (ρ_{CO2}) and CO_2 mole fraction (x_{CO2}) on mean particle diameters (MPD) with standard deviations (SD) and yields of processed lignins using the clCO$_2$ antisolvent.[a]

Entry	Sample	T (K)	P (MPa)	C_{lign}[b] (wt%)	$F_{sol'n}$ (kg/h)	ρ_{CO2}[c] (kg/m³)	x_{CO2}	MPD[d] (nm)	SD[e] (nm)	Yield[f] (%)
1	PKL-1	280.2	15.0	5.3	0.06	968.24	0.99	38.0	7.2	77.3
2	PKL-2	288.2	15.0	5.3	0.06	927.77	0.99	51.0	9.8	75.0
3	PKL-3	298.2	15.0	5.3	0.06	876.47	0.98	53.6	11.2	70.0
4	PKL-4	280.2	7.5	5.3	0.06	917.75	0.94	38.0	11.9	75.0
5	PKL-5	288.2	7.5	5.3	0.06	862.05	0.92	47.0	12.8	67.5
6	PKL-6	298.2	7.5	5.3	0.06	761.87	0.90	74.0	17.3	59.0
7	PKL-7	280.2	15.0	5.3	0.03	968.24	0.99	43.0	17.5	51.0
8	PKL-8	280.2	15.0	10.6	0.06	968.24	0.99	54.5	10.7	88.3

[a] Feed flow rate of CO_2 (antisolvent) was fixed at 3.0 kg/h for all entries. [b] The lignin/DMF systems with different concentrations. [c] http://webbook.nist.gov/chemistry/ [d] Measured from FESEM images. [e] Standard deviation of particle size. [f] Yield of processed lignin collected on the filter paper.
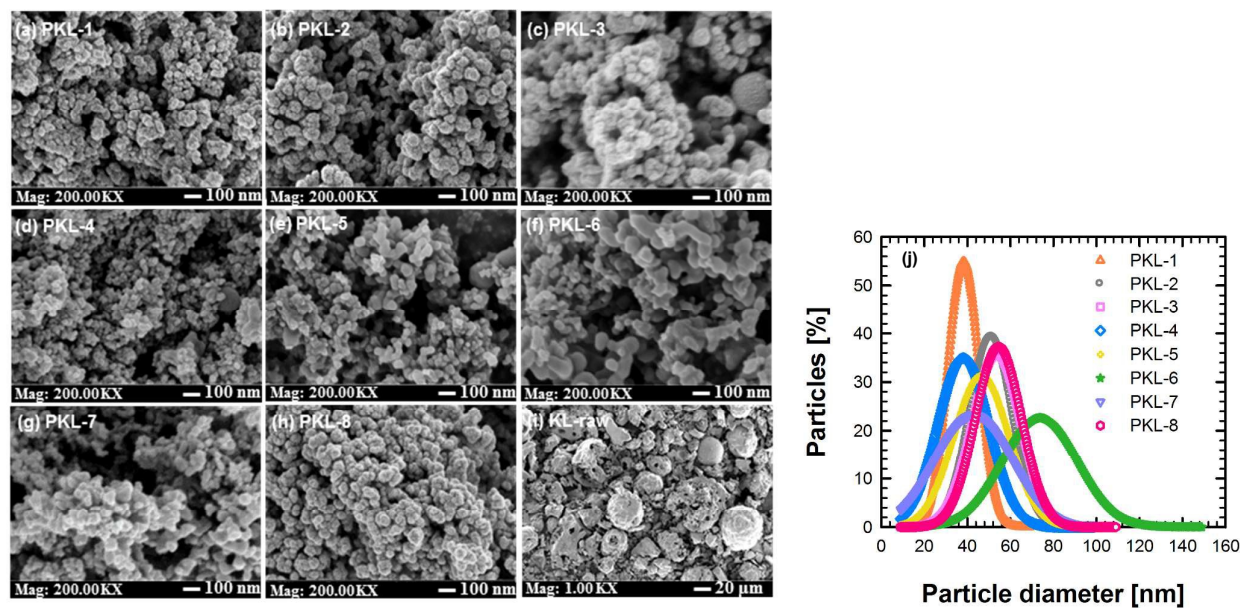

Fig. 2 FESEM images of the processed lignins obtained from various experimental conditions with the clCO$_2$ antisolvent (a-h); raw lignin (i); and particle size distributions of the various processed lignin nanoparticles measured on their respective FESEM image (j).

processes.[61,62] This phenomena was postulated by Reverchon and co-workers[62] that the coalescence was due to the formation of solid bridges, connecting groups of nanoparticles, due to the fact that nanoparticles contained or were in contact with small quantities of solvent. By the other hand, the pressure effect on particle morphology, size and distribution is more significant at high process temperature rather than in the case of working at low temperature. At the low temperatures of 280.2 K and 288.2 K, for instance, if the pressure was increased 7.5 MPa to 15.0 MPa the coalescence of nanoparticles disappeared whereas the mean diameter of particles were unaffected (approximately 38 nm for both conditions), see PKL-1 vs PKL-4 (at 280.2 K) and PKL-2 vs PKL-5 (288.2 K) presented in Table 1 and Fig. 2. In contrast, a marked decrease in mean diameter of particles (from 74 nm to 54 nm) with a narrower particle size distribution was observed at high temperature of 298.2 K when the pressure is increased 7.5 MPa to 15.0 MPa, see PKL-3 vs PKL-6 shown in Table 1 and Fig. 2. In other words, this coalescence effect is clearly evident in the case at high temperature (298.2 K) and low pressure (7.5 MPa), where the density of CO_2 was lowest (761.87 kg/m^3), see PKL-6 in Fig. 2(f), suggesting temperature has a rather important effect on the aggregation and coalescing extent. This is likely due to the effect of temperature on all the elementary phenomena responsible for the ultimate extent of aggregation or coalescing achieved. Furthermore, it is obvious that for a range of pressure and temperature equivalent to CO_2 densities from 862.05 to 968.24 kg/m^3, the mean particle diameter remained constantly less than 55 nm, with ranges being between 47 and 65 nm (Table 1) but particles of morphologies were affected. It is also evident that this coalescence phenomena can be controlled by the precipitation pressure; there is no formation of the coalesced nanoparticles at high pressure of 15.0 MPa for the studied temperature ranges, and consequently smaller and uniform with non-connected quasi-spherical nanoparticles were generated. It is worthwhile to note that the density of CO_2 corresponding to the couple parameters of temperature and pressure can definitely influence on the morphology, size and distribution of the lignin nanoparticles formed using clCO$_2$ as an antisolvent. As a result, the smallest size with defined quasi-spherical nanoparticles, PKL-1 depicted in Fig. 2(a), were achieved when the experiment performed at low temperature (280.2 K) and high pressure (15.0 MPa), where density of CO_2 was highest (968.24 kg/m^3). As indicated in Fig. 2(j) and Table 1, the mean diameter of particles are very small, approximately 38 nm, and had a sharp size distribution.

Further, experiments were carried out at two solution flow rates: 0.03 and 0.06 kg/h, to examine the effect of solution flow rate on the particulate products while keeping constant at other parameters: temperature was 280.2 K; pressure was 15.0 MPa; and initial lignin concentration was 5.3 wt%. It is clear that the flow rate of sprayed solution is impact on the

morphology, size and size distribution of the processed lignin nanoparticles, in agreement with other reports for different type of materials.[40,63] For example, as a decrease of the solution flow rate an increase of the mean particle size and an enlargement of the particle size distribution was observed: from 38 to 43 nm for mean particle diameter and from 7.2 to 17.5 nm for the standard deviation of the particle size distribution, see PKL-1 vs PKL-7 presented in Fig. 2(j) and Table 1. FESEM images in Fig. 2(a) and (g) also clearly show the nanoparticles of PKL-7 were larger size with aggregated and coalesced each other as opposed to those of PKL-1, which were smaller and uniform with moderately dispersed nanoparticles.

The influence of solute concentration was studied with two various initial lignin concentration in the solution such as 5.3 and 10.6 wt%; at the same temperature of 280.2 K, pressure of 15.0 MPa and solution flow rate of 0.06 kg/h. The dependence on the concentration of the liquid solution is evident: the increase of the solute concentration in the liquid phase produced an increase of mean size with an enlargement of size distribution, see PKL-1 vs PKL-8 in Fig. 2(j) and Table 1. The mean particle diameter and standard deviation of size distribution for PKL-1 were 38.0 nm and 7.2 nm whereas those for PKL-8 were 55.4 nm and 11.5 nm, respectively. In addition, FESEM images in Fig. 2(a) and (h) reveal the nanoparticles of PKL-8 were found to be a slightly larger and more aggregated quasi-spherical nanoparticles as compared to those of PKL-1. This solute concentration effect is a good agreement with the results obtained from previous reports for producing different materials using PCA or SAS processes.[42,63,64]

Surface area, pore size and distribution. As is known[65] that the range of specific surface area can vary widely depending on the particle size, shape and porosity. Smaller particles have higher surface area. In addition to particle size, the particles shape contributes to the surface area of the powder. Obviously, the influence of pores can often overwhelm the size and, the external shape factors.

In order to get a more information and hence precise results on the influence of process parameters on the particle morphology, size and distribution, the textural properties of the lignin nanoparticles produced by the clCO$_2$ antisolvent were analyzed by nitrogen sorption. Nitrogen adsorption-desorption isotherms and corresponding pore size distributions of the processed lignin nanoparticles are presented in Fig. 3(A and B), respectively. All isotherms are type IV characteristics with a significant type H3 loop, shown in Fig. 3A. The type VI isotherms are very typical of mesoporous materials. A broad hysteresis loop was always present, which is associated with the secondary process of capillary condensation and results in the complete filling of the mesoporous at high relative pressure.[66–69] The type H3 loop, which does not clearly exhibit any adsorption plateau at relative pressures close to unity, is usually related to existence

of slit-shape pores in materials.[70] It is also indicative of a pore size distribution extending into the macrospore range, a fact which is also clear from the FESEM images in Fig. 2. The very low amount of nitrogen adsorbed at low relative pressure indicates the nearly absence of microporosity.
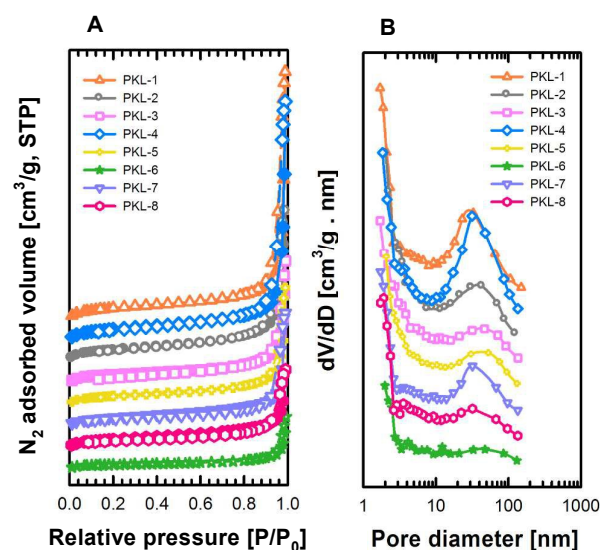

Fig. 3 Nitrogen sorption isotherms of the various processed lignin nanoparticles (A); and the corresponding pore size distributions (B). Closed symbol: adsorption, open symbol: desorption. Pore size distributions were calculated by the BJH method from the desorption branches.

The textural characteristics of the processed lignin nanoparticles determined by nitrogen sorption analysis are presented in Table 2. For a comparison purpose, analysis of the raw lignin was carried out and the results obtained are also shown in Table 2. As expected, a remarkable influence of the operational parameters on the particle textural properties of the processed lignin nanoparticles were observed. In all cases, BET surface areas of the lignin nanoparticles ranged from 34 to 92 m^2/g whereas that of the raw lignin was only about 0.2 m^2/g. Under the same conditions, the BET surface area of the lignin nanoparticles decreased with increasing temperature and initial lignin concentration as well as decreasing pressure and solution flow rate. In addition, it clearly exhibits that the smaller size and less aggregated nanoparticles had higher surface area as opposed to larger size with more aggregated/ coalesced nanoparticles, which had considerably lower surface area. For example, PKL-1, which consists of the uniform and smallest size with moderately dispersed lignin nanoparticles, had relatively high surface area of up to 92 m^2/g. On the contrary, PKL-6, which represents largest size and more

aggregated/coalesced nanoparticles, had lowest value of 34 m^2/g. It is noteworthy that the surface area results are well agreement with the results obtained from the corresponding FESEM morphological characterization. It is apparent that the mesopore surface area of lignin nanoparticles estimated by the *t*-plot method essentially corresponds to the BET surface area. This further verified that the porosity of the processed lignin nanoparticles mainly due to the contribution of mesopores since the micropore volume is almost negligible, presented in Table 2.

Table 2 BET surface areas (S_{BET}), mesopore surface areas (S_{meso}), total pore volumes (V_{Tot}), micropore volumes (V_{mic}) and average pore diameters (D_{avg}) of raw and various processed lignin nanoparticles.

Sample	S_{BET} (m^2/g)	S_{meso} (m^2/g)	V_{Tot} (cm^3/g)	V_{mic} (cm^3/g)	D_{avg}[a] (nm)
KL-raw	0.2	00.0	0.0000	0.0000	-
PKL-1	91.6	87.7	0.4134	0.0000	21.1
PKL-2	78.4	73.0	0.1481	0.0012	19.9
PKL-3	61.3	47.1	0.1188	0.0060	19.3
PKL-4	79.7	75.7	0.2056	0.0005	27.5
PKL-5	61.7	56.0	0.1133	0.0017	21.5
PKL-6	34.3	25.1	0.0497	0.0038	20.8
PKL-7	59.0	58.9	0.2554	0.0000	20.9
PKL-8	54.8	54.7	0.1766	0.0000	16.1

[a] Obtained from BJH desorption branches.

More information about the pore structure of the lignin nanoparticles (PKL-1 and PKL-8) as compared to the raw lignin (KL-raw) are revealed by HRTEM. As can be seen in Fig. 4, the particles of PKL-1 and PKL-8 have a uniform structure with a well-developed three-dimensional network consisting of roughly spherical lignin particles whereas that of KL-raw had an irregular dense/solid structure, indicating in an agreement with the results of above pore structure analysis. Especially, the utilization of clCO$_2$ may be lead to the formation of many inerratic nanoparticles because of the diffusion effect. The estimated diameters of the spherical particles of PKL-1 are around 19–28 nm, see insert Fig. 4(b). As is known that these primary particles are cross-linked with each other to form the abundant textural mesopores in the organic aerogels.[66–69] Therefore, the pore textural properties of lignin is of greatly important parameters as its applications in the preparation of organic aerogels due to which can directly determine on the final material's properties.
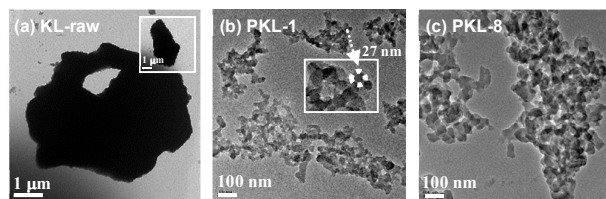
Fig. 4 HRTEM images of the raw lignin: KL-raw (a) and processed lignin nanoparticles: PKL-1 (b) and PKL-8 (c). Insert figure in (b) is the high resolution image of a specific area.

The mechanisms of lignin nanoparticles formation

The above results show that temperature, pressure, solution flow rate and initial lignin concentration are all the main factors affecting the formation of lignin nanoparticles using $clCO_2$ as an antisolvent. We then attempted to explain the possible reasons. The changes of the lignin nanoparticles' morphology, size and size distribution by different process parameters were discussed in terms of their BET surface area values since which is more precise quantitative data rather than the results of particle size measurements obtained on FESEM images, especially in case of coalescent particles. The effect of temperature and pressure can be explained by taking into a consideration of the degree of mutual solubility between DMF and CO_2 under the operating conditions. Fig. 5 shows the HSP distances (R_a) of DMF in CO_2 and vice versa, and BET surface area of the processed lignin nanoparticles as a function of density of CO_2 at different operational temperatures and pressures. It is apparently to observe that at the same pressure, as the temperature increased; the density of CO_2 decreased, the distance between DMF and CO_2 was longer, and a lower value of BET surface area for the processed nanoparticles was achieved. It is attributed that the decrease in mutual solubility of DMF and CO_2 induced to a lesser supersaturation for the solute. As a consequence, a larger size of aggregated/ coalesced with a broader size distribution of nanoparticles were achieved due to probably the prevailing of particle growth followed by the lesser rate of particle nucleation. At the same temperature, on the other hand, when the pressure was decreased from 15.0 MPa to 7.5 MPa the distance between DMF and CO_2 was longer in accordance with the decrease of density of CO_2, and then lower value of BET surface area for the nanoparticles was observed. It is important to notice that the morphologies of the nanoparticles obtained at low pressure of 7.5 MPa were an irregular size of aggregated and coalesced, and had a wider size distribution whereas those of nanoparticles formed at high pressure at 15.0 MPa show more uniform size of moderately dispersed with a narrower size distribution. Indeed, this coalescence of particles was very significant at the high temperature and low pressure, in which the long distance between DMF and CO_2 and the lowest density of CO_2 was observed as can be clearly seen in Fig. 5 (the values in dotted circles). This is evidently

agreed with the proposed phenomena for supercritical antisolvent precipitation reported by Reverchon et al.[62] that the coalescence is produced by the interaction of DMF dissolved in the CO_2 and the lignin nanoparticles at low pressure due to the presence of small quantities solvent in the solid nanoparticles. The increase of pressure increases the strength of solvato-complex formed between DMF and CO_2, thus reducing the ability of DMF of interacting with lignin nanoparticles.

By the other hand, this might be attributed to the movement of the MCP to higher pressures and enlargement of the two-phase region, caused by the reduction of affinity between DMF and CO_2 because of the presence of the lignin as a third component, as the most common effect found in SAS process.[64] It is also worth noting that a few numbers of big spherical nanoparticles were observed on the FESEM images for some cases, especially operating at all case of low pressure for various temperatures, and only the case of high temperature and high pressure, as can be seen in Fig. 2(c, d-f), It can be explained, according to the proposed mechanism for a PCA process by Ṕerez de Diego et al.[41] for operating conditions at above critical pressure of the mixture solvent-CO_2 or spraying over liquid CO_2, that droplets of a polymer rich-phase might be formed as results of a liquid-liquid phase split induced in the polymer solution when it got in contact with the CO_2 even if the operating conditions were in a single liquid state in the system and no droplets formation by our visual observation at the exit of nozzle through the operations. Afterwards, the polymer-rich phase droplets are formed inside each solution droplet. These polymer-rich phase droplets may agglomerate inside each solution droplet and form an interconnected network. As the DMF is extracted by the CO_2, these polymer-rich domains solidify. If the solution droplets are stable enough, polymer solidifies on the droplets surface and the structure of the original solution droplets is maintained. It is also evident that this particle coalescing phenomena can be overcome by increasing the pressure to 15.0 MPa at the same temperature. For example, at the low temperature (280.2 K) and high pressure (15.0 MPa); where the density of CO_2 was the highest (968.24 kg/m^3), the distance between DMF and CO_2 was the shortest and the maximum value of BET surface area for the nanoparticles was obtained. As a consequence, the smallest size, uniform, and moderately dispersed quasi-spherical shape with narrow size distribution of nanoparticles (see PKL-1 in Fig. 2a) were formed. This highlighted that pressure is essentially prerequisite to be far above from the critical pressure of the MCP of the DMF-CO_2 system in order to ensure immiscibility of the solution and the stream of liquid CO_2. In this case, the formation of nanoparticles has been attributed to rapid mass transfer effects resulting from the turbulent mixing between the fully miscible solution and the liquid CO_2 stream in absence of droplets.[44] Accordingly, they are formed following the classical crystallization scheme of primary homogeneous nucleation and growth from a higher maximum supersaturated solution simultaneously.[71] It is also interesting to observe that the shape of lignin nanoparticles resemble with the typical

characteristics of nanoparticles, which are produced at pressure far from the MCP such as 15.0 MPa, from several different materials using SAS processes.[51,64,72–74] The surface of nanoparticles did not present substructure. It was relevant that, they did not collapse on the bottom of the vessel; but presented a high volume fractal-like geometry,[59] that can be destroyed during the powder collection.
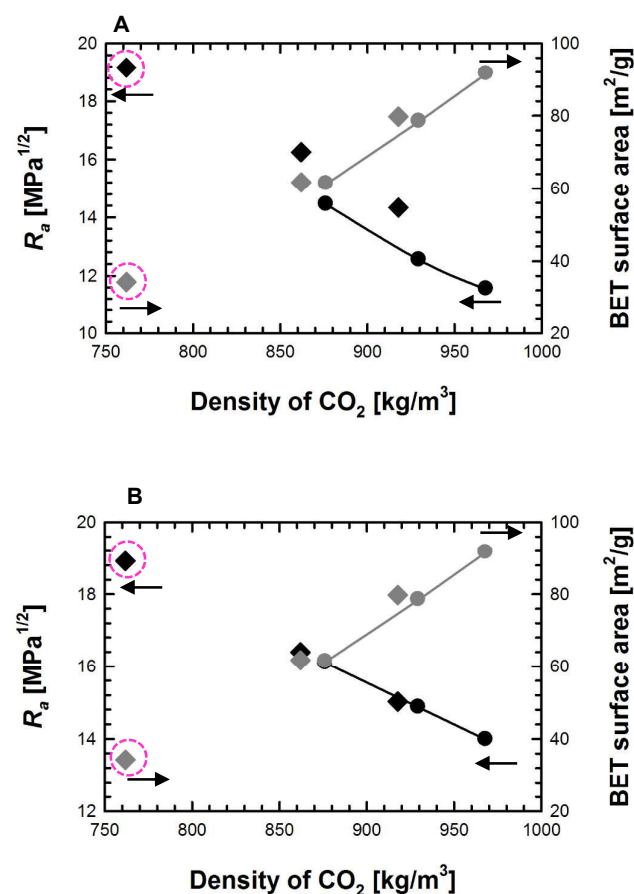

Fig. 5 The HSP distance (R_a) of DMF in CO_2 (A) and vice versa (B) and BET surface area of the processed lignin nanoparticles as a function of density of CO_2 at different operational temperatures and pressures. Black and grey circles with line represent for the data obtained from different temperatures (280.2 K, 288.2 K and 298.2 K) at 15.0 MPa. Black and grey diamonds represent for the data obtained from different temperatures (280.2 K, 288.2 K and 298.2 K) at 7.5 MPa.

Furthermore, the increase of particle size and the broadening of the size distribution with decreasing solution flow rate, see PKL-1 vs PKL-7 shown in Fig. 2, seems to be by the impact of particle growth dominated over nucleation rate. This is likely due to the precipitation of the solute occurs earlier in time during the expansion process; where very fact supersaturation reaches sooner as the interaction with liquid CO_2 and the solution, resulting in increased time for particle growth and consequently larger size with wider size distribution of nanoparticles produced. Especially, the particles of coalescence formed at slow solution flow rate can be understood by the heterogeneous mixing favoring to the primary heterogeneous nucleation induced by other surface as the common effect in classical nucleation theory.[71] Nucleation on a foreign surface, which has a lower surface energy than that of a new solute particle, takes place at a lower critical supersaturation and thereby lead to reduction of affinity between DMF and CO_2 because of the presence of the lignin as the foreign surface. Thus, the presence of small quantities of DMF in the lignin nanoparticles that, when they collided in the colloidal suspension, formed a liquid bridge that upon drying produced the solid connection among groups of them.

An explanation of the effect of initial lignin concentration on the particle formation phenomena is that at the high lignin concentration, precipitation of the lignin occurs earlier during the expansion process because of the supersaturation reached very fast to the maximum saturation line as soon as the contact with liquid CO_2, resulting in increased time for crystal growth and thereby nanoparticles of more aggregated and larger size with wider size distribution were obtained (see PKL-1 vs PKL-8 in Fig. 2). It can be explained by another way, according to the classical nucleation theory, that there might be occurred secondary nucleation results from the presence of earlier precipitated particles present in the solution. Contemporary reviews[75,76] have classified secondary nucleation into three categories: apparent, true and contact. In our case is similar to true secondary nucleation: which occurs when the current level of supersaturation is higher than the critical level for the solute particles present in the solution. This is very common mechanism when ripening plays a role in the crystal growth process. On the other hand, this size increase can be due to a brownian motion. Higher concentration can produce a greater supersaturation, which can make small particles precipitate. However, if more nuclei are formed, more collisions can be produced between the nuclei, giving as a result more aggregate and single particles with a larger size.[77] On the contrary, at the low lignin concentration, precipitation of the lignin is reached later during the expansion process; hence nucleation is the prevailing mechanism giving smaller particles with a narrower size distribution. In addition, more uniformly distributed nanoparticles were achieved at low concentration, since high initial supersaturation was reached which lead to primary homogeneous nucleation for the solute. It is worthwhile to note that at high concentration, there is no formation of fibrils as like other reports for PCA process,[34,35,38,40,51] indicating this concentration is still being a favorable ranges for particle formation under the studied conditions and likely due to the intrinsic chemical nature of lignin. One more possible reason is warm-cold situation, *i.e.,* solution temperature (298.2 K) > the process temperature (280.2 K), might be favorable to the process performance, since it combines potential high supersaturation ratio, fast mixing between solvent and antisolvent and opportunity to process concentrated solutions.[55,78]

Characteristics of lignin nanoparticles

In order to examine and compare the effects of process parameters on the chemical structural features of the lignin nanoparticles formed using $clCO_2$ as an antisolvent, ATR-FTIR analysis were performed on all processed lignin samples and the raw kraft lignin (KL-raw) as a reference. The absorbances are normalized to 1 at 1511–1512 cm^{-1} which is assigned to the maximum absorbance peak of the aromatic skeleton stretch in studied samples. Condensation indices (*CI*) of the samples, which is attributed to the degree of formation of new C–C linkages in the course of secondary reactions depending on the severity of isolation, were calculated as an equation suggested by Faxi.[79] The assignments of the major bands, peak positions, absorption intensities and *CI* values are summarized in Table S3† and FTIR spectra acquired were also depicted in Fig. S2†. The FTIR spectrum of the KL-raw contained characteristic absorption bands of guaiacyl unit: 1267–1266 cm^{-1}, 1126–1140 cm^{-1}, 1033–1031 cm^{-1}, 856–854 cm^{-1}, 816–814 cm^{-1} and there is no absorption of syringyl bands in the spectra, indicating which seemed to be derived from softwood and a strongly consistent results with other softwood lignins.[80,81] In comparison to the KL-raw, all the spectra for the processed lignin samples consisted of the absorption bands characteristic of aromatic structures: O–H stretching band (3380–3365 cm^{-1}), C–H stretching band (2840–2940 cm^{-1}) and aromatic skeleton stretching band (~1600, 1152–1151 and 1425–1422 cm^{-1}), suggesting no significant impacts on the structures of samples with the PCA process. However, it is notable that the somewhat higher *CI* values for almost processed samples; except PKL-1, than that of the KL-raw. The increase in *CI* of the processed samples resulted by the values of the less minima and less maxima in the whole spectra range as compared to the KL-raw, shown in Table S3†. It is assumed that the formation of an α-1 linkage according to the β-1 free radical coupling reaction by the elimination of side chain[82] and/or of diphenyl methane linkage by free phenolic hydroxyl groups might react with formaldehyde from DMF occurred in the dissolution process.[83] Additionally, the increase in the intensity at 1653–1657 cm^{-1} for all processed samples which is ascribed due to the increase of water in lignin[84] and/or might arise from the change in C=O bond moment as a consequence of the adulterine of any residual DMF on complex formation of phenols in lignin.[85] It is evidently to observe that this absorption peak of the PKL-7 formed at low temperature, high pressure and slow solution flow rate is highly visible than others, implying that the high absorption of water associated with high remained residual DMF in the lignin nanoparticles. It is also highlighted that particle morphology, size and size distribution is a good correlation with its chemical structure. The FTIR spectrum of the PKL-1: uniform, smallest and more dispersed nanoparticles among the studied samples, has intense absorption bands corresponding to O–H stretching of phenolic and aliphatic moieties (at ~3378 cm^{-1} and ~1379 cm^{-1}), water absorption (at ~1657 cm^{-1}), C–C stretching of aromatic skeleton (at ~1596 cm^{-1}) and C=O stretching in guaiacyl unit (at ~1267 cm^{-1}) which are

shown as red sphere marks in Fig. 6, indicating the particle surface modified with higher phenolic hydroxyl and carboxyl functional groups as compared to the raw lignin, which are responsible for enhancing solubility and stability of lignin nanoparticles. Thus, the other important physicochemical and thermal characteristics were further investigated for the PKL-1 in order to gain more detail information of the quality of the nanoparticles. The same characterization for the KL-raw was also carried out as a reference.

The X-ray photoelectron spectroscopy (XPS) survey spectrum of the KL-raw exhibits the presence of C 1s, O 1s, Na 1s and S 2p core levels while the disappearance of Na 1s and S 2p was found for that of PKL-1 (Fig. S3†). As the results of elemental compositions calculated from spectra survey presented in Table S4†, the KL-raw is contaminated with Na (11.6%) and S (0.7%), presumable resulting from its preparation in the kraft process, as observed previously elsewhere.[86] The C/O ratio for the KL-raw and PKL-1 were 2.5 and 3.1, respectively which is probably due to the selectively extraction of aromatic hydrocarbons by DMF during dissolving process.[87] The analysis of these spectra clearly demonstrates significant changes in chemical state of lignin before and after the PCA process. The core level spectra of C 1s and O 1s with fitting data for the KL-raw and PKL-1 are presented in Fig. 7 and the relative surface functional group compositions obtained by the binding energies of component peaks in C 1s and O 1s signals are summarized in Table S5†. The PKL-1 composed of higher contents of C–O–C, C–OH, Ph–OH and C–O groups whereas the profound contents of C–C, C–H, O=C–OH, Ph=O, Ph–C=O and O–O groups appeared in the KL-raw, confirming which is good correlated with its FTIR results.
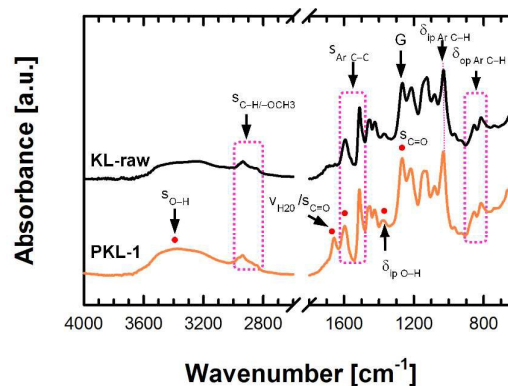

Fig. 6 ATR-FTIR spectra of the raw lignin: KL-raw, and processed lignin nanoparticles: PKL-1. The red spheres indicate intense absorption peaks for the PKL-1 as compared to the raw lignin. s: stretching; v: vibration; G: guaiacyl unit; s_{Ar}: stretching of aromatic skeleton; δ_{ipO-H}: O–H in-plane deformation in phenolic OH; $\delta_{ipArC-H}$: aromatic C–H in-plane deformation of G; $\delta_{opArC-H}$: aromatic C–H out-of-plane deformation of G.
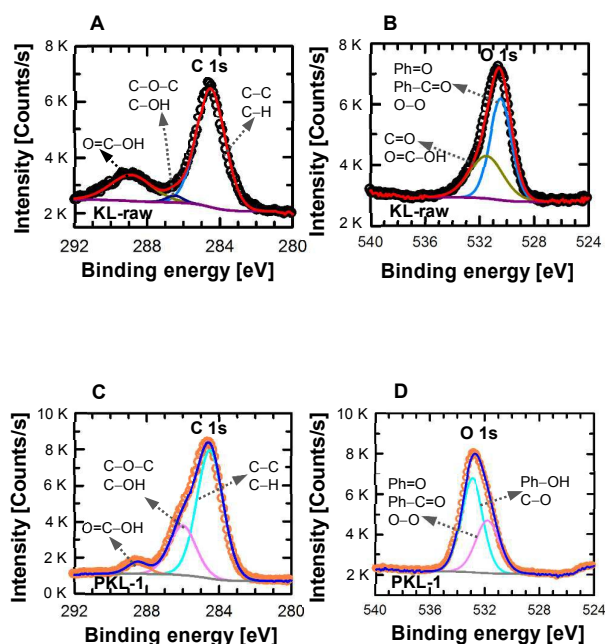
Fig. 7 Core level XPS spectra C 1s and O 1s for the raw lignin: KL-raw (A, B) and lignin nanoparticles: PKL-1 (C, D).

degradation stages in Fig. 8C. According to the literature,[93] the first stage was observed below 373.2 K with sharp peaks on the DTG curves at 326.5 and 363.6 K for KL-raw (4.0%) and PKL-1 (4.7%), indicating to the desorption of water molecules adsorbed on the surface of the lignin particles. The second stage which is ascribed the main lignin degradation, was observed a broad temperature range between 410 and 873 K with a maximum degradation temperature, T_d at about 592 K for both samples. In this stage, a shoulder peak region occurred in temperature range between 410 and 473 K for both samples, which are 6.7% for KL-raw and 8.2% for PKL-1 at 473 K, is ascribed to the volatilization of low molecular mass of monomeric compounds. Chu et al.,[94] have also suggested that the lignin oligomeric compounds don't decompose under 523 K. As regards the % degradation at 473–873 K, the value for both samples are quite similar: 48.2% for KL-raw and 49.8% at 873 K, and consistent with values reported[94] for other lignins, which are in the range of 40–60%. The slow degradation rate was observed in the third stage at temperature range between 873–1073 K, in which the charring process start at around 873 K with the evaluation of methane and then taps off around 1073 K but charring process still continues after until 1223 K.[95,96] It is worthy to observe that the solid residues at 1073 K for both samples were nearly identical: 45.3% for KL-raw and 45.5% for PKL-1, which are comparable with previous report for the kraft lignin.[97] It is believed that the lignin nanoparticles belong to a comparable thermal stability and higher purity in terms of Na and S contents than the KL-raw.

On the other hand, the XRD pattern of the PKL-1 shows low intensity with a large broad amorphous region (centred at 2θ = 23.4°) as compared to the KL-raw (Fig. 8A), which suggests that the lignin nanoparticles has less crystallization degree than the raw lignin. This is likely due to the smaller in particle size of nanoparticles and plasticization by sorption of water from the environment.[88] Since it is well known that water can readily enter amorphous regions of solids and acts as a plasticizing agent. Once incorporated into an amorphous region, water can increase the free volume and lead to enhanced molecular mobility of the solid causing a reduction in the glass transition temperature, T_g. As is shown in Fig. 8B, the T_g of the KL-raw was found to be 419.9 K which is comparable with reported data.[89] As we expected, the T_g of the PKL-1 shifted to the low temperature of 386.2 K which is attributed to specific sorption of plasticizers, such as water, are very efficient in low content because of their functionality and accessibility to sorption sites.[90] In other hand, the increased T_g of KL-raw seemed resulting from the presence of alkali metal (Na) in lignin, which led to cause the cross-linking through condensation as previous reports.[91,92] In addition, the TG/DTG profile in Fig. 8C apparently exhibits the DTG curve of the PKL-1 contained two distinct peaks while that of the KL-raw has several peaks. This can be attributed that the PKL-1 has more uniformity of thermal degradation as compared to the KL-raw. The thermal behaviors the samples can be explained by dividing three
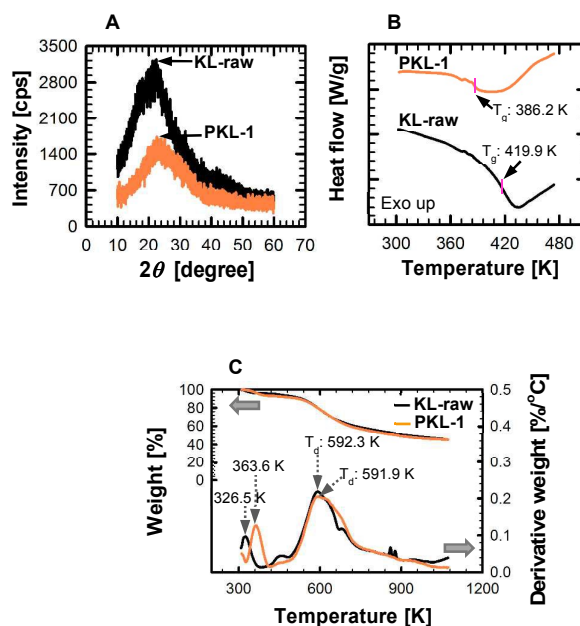

Fig. 8 XRD patterns (A); and thermograms of DSC (B) and TG/TDG (C) for the raw lignin: KL-raw, and processed lignin nanoparticles: PKL-1.

The UV-vis absorption spectra for the samples shown in Fig. 9A further confirmed that the PKL-1 has substantially high UV absorption in comparison to the KL-raw. The absorption peaks at about 280 nm are designated the $\pi-\pi*$ transition of the characteristics of the guaiacyl structural units in lignin.[98] The broad shoulder band of the samples at maximum wavelength of about 330 nm are due to the associated hydroxycinnamic acids (such as ferulic and *p*-coumaric acids),[99] which are known to be potent antioxidants.[100] It is also evident that the PKL-1 was well suspended in water at room temperature until for 24 h but the almost particles of KL-raw rapidly settled down within 30 min (Fig. 9B and the digital photographs for PKL-1 illustrated in Fig. S4†), indicating the lignin nanoparticles are monodispersed particles and have highly dispersion stability. The dissolution profile for the samples in Fig. 9C clearly displays the PKL-1 has the enhanced dissolution rate (3.1 folds), which reached the dissolution equilibrium within 1 h, but the KL-raw didn't reach its dissolution equilibrium until 5 h. This enhanced solubility is due reflected by the effectively surface modified with high functional groups of hydroxyl, carbonyl and/or carboxylic on the nanosized particles resulted using the clCO$_2$ antisolvent.
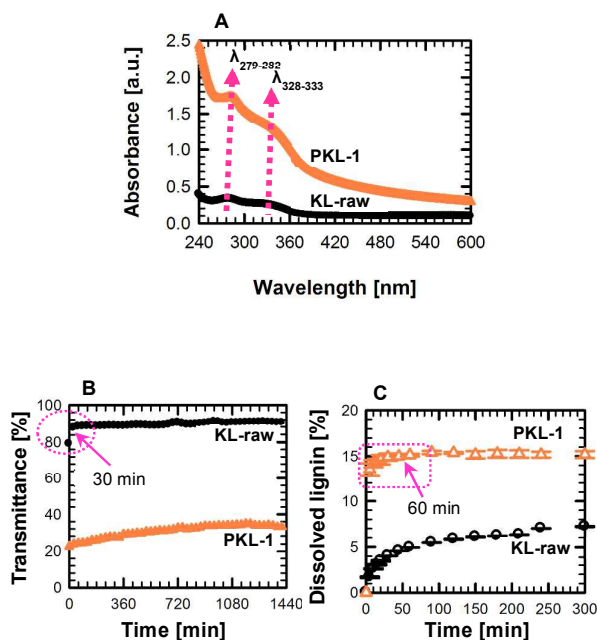

Fig. 9 UV-vis spectra (A); percent in intensities of UV transmittance measured at wavelength 400 nm with respect to retention time (B); and dissolution profile (C) for the raw lignin: KL-raw, and processed lignin nanoparticles: PKL-1.

Moreover, it is noteworthy to observe that significant differences of lignin particle stability depending on pH of the aqueous solutions before and after the PCA process is

shown in Fig. 10(A and B). The UV-vis spectrum of the KL-raw (Fig. 10A) showed the absorbance intensity didn't change much with increasing of pH from 2 to 9 but it extremely raised up when pH was increased to 10, indicating that the KL-raw dissolved under pH 10. However, the PKL-1 was stable at slightly acidic (pH 3−4), neutral (pH 6−7) and basic (pH 8−9) conditions as is shown in Fig. 10B, which is attributed to the electrostatic mechanism depending on pH in the solution.[101] In addition, the significant descent in intensity at pH 10 was likely due to the aggregation and precipitation of the particles in the solution which is reversal mechanism as compared with the KL-raw. Indeed, the pH-response properties of PKL-1 is beneficial for its applications as bionanomaterials.[102]
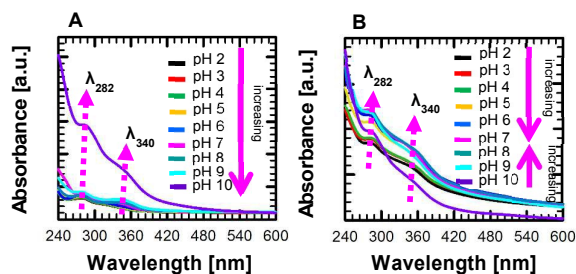

Fig. 10 UV-vis spectra of the raw lignin: KL-raw (A) and processed lignin nanoparticles: PKL-1 (B) at various pH values.

Cytotoxicity of lignin nanoparticles

Due to the release of nanoparticles results in cytotoxicity on cells by compromising the integrity of the cell membrane[103] and their environmental concerns,[104] it is a crucial issue to evaluate their biocompatibility and biodegradability nowadays. Therefore, a derivative of *Pseudomonas aeruginosa* tagged with green fluorescent protein (PAO1 GFP) was employed as a model bacteria to investigate the biocompatibility of the processed lignin nanoparticles (PKL-1) to assess the prospects of the lignin nanoparticles as applications in nanomaterials such as cosmetic and pharmaceutical formulations, and drug delivery system. The cell viability of the PKL-1 was determined by a plate count method and UV-vis assay in terms of lignin degradability. The same experiments were performed for the KL-raw and only PBS solution without lignin as a comparison with the PKL-1 and a control, respectively. As can be seen in Fig. 11(A), the populations of PAO1 GFP growth in the both lignin solutions were higher than that in the control one. Specifically, the PKL-1 showed the growth rate was faster during a short incubation time (up to 6h) and then it slowed down for the longer time as compared to the KL-raw. On the other hand, the UV-vis assay results in Fig. 11(B) revealed the decrease in intensities for both solutions measured at maximum wavelength of 280 nm, which is known as the

presence of soluble lignin in the filtrated samples, as the increase in time elapsed. Indeed, the fast decreasing intensities in a short incubation time (up to 6 h) were observed for the PKL-1, which is consistent with the population growth studies. These studies suggested that the lignin nanoparticles demonstrated no cytotoxicity and were possibility to degrade by the studied bacteria.
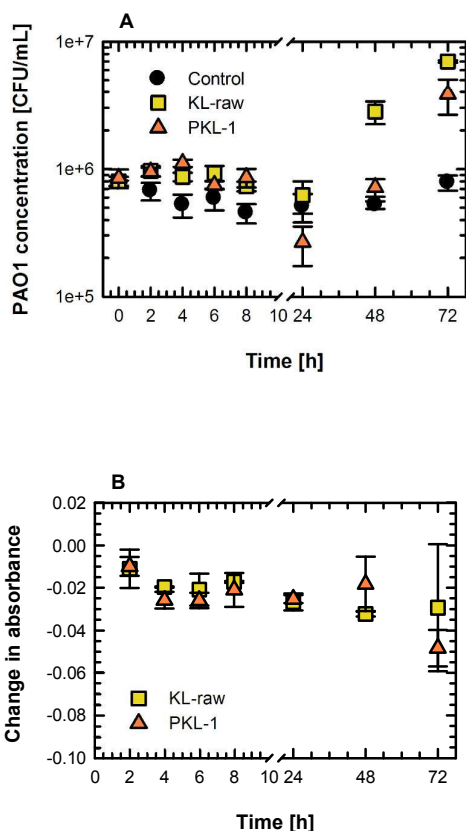

Fig. 11 PAO1 GFP growth rates in lignin solutions (KL-raw and PKL-1) and control (PBS) with respect to incubation time (A); and their absorbance changes at λ_{280} for the filtered samples (B) incubated with PAO1 GFP at 310.2 K and 120 rpm.

Furthermore, the CLSM images for both samples and control were acquired at incubation time for 0 h and 24 h, presented in Fig. 12. Through these images, it was observed that the distributions of PAO1 GFP in the suspended lignin nanoparticles solution for initial (0 h) and 24 h were similar which can be compared with the KL-raw and control images. This results further confirmed that the lignin nanoparticles are biocompatible with the PAO1 GFP.
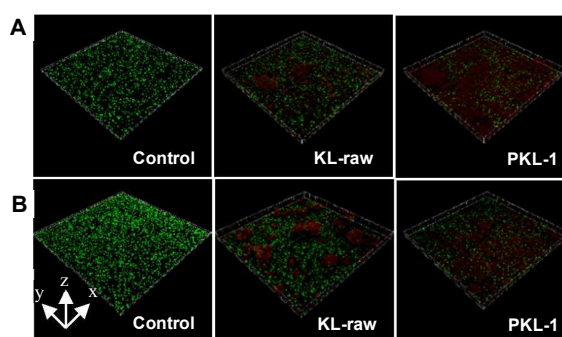

Fig. 12 CLSM images for control: PBS solution, raw lignin: KL-raw, and processed lignin nanoparticles: PKL-1, incubated with PAO1 GFP for 0 h (A) and 24 h (B) at 310.2 K and 120 rpm. The scales for x, y and z axes were 42.3 μm, 42.3 μm and 5.5 μm, respectively. Green color: live PAO1 GFP; dark red lumps: lignin particles.

Experimental methods

Materials

N,N−Dimethylformamide (DMF, 99.5%), sodium hydroxide (NaOH, 98.0%) in bead form, hydrochloric acid (HCl, 35−37%) were purchased from Samchun Pure Chemical Co. Ltd., Korea. Carbon dioxide (CO_2, 99.99%) and nitrogen (N_2, 99.999%) were obtained from Hyup-Shin Gas Industry Co. Ltd., Korea. Kraft (alkali) lignin was purchased from Sigma-Aldrich, USA, and used as received. Deionized water (DI) was prepared by a Milli-Q water-purification system (Millipore, Bedford, MA, USA) and used in all experiments.

Lignin nanoparticles preparation using a compressed CO_2 antisolvent method

An apparatus used for performing the experiments with clCO_2 as an antisolvent is shown in Fig. S5†. The apparatus was mainly composed of two high-pressure plunger pumps to supply CO_2 and target sample solution, a precipitating vessel, a filter, and a separator. The precipitating vessel (SUS316 cell, width: 0.115 m, length: 0.095 m, height: 0.24 m, diameter: 0.003 m, volume: 60 mL) was assembled with two heat transfer jackets and a sapphire window to view the precipitation process. The operating temperature was measured using two K-type thermocouples and recorded with a strip chart recorder (μR 100, Yokogawa, Japan). The operation pressure was controlled by a pressure regulator (26-1721-24, TESCOM, USA).

As the experimental detail, the CO_2 was initially delivered by pumping at a specified flow rate to the precipitator through a cooler at 258.2 K (MC-11, JEIO TECH, Korea) to ensure the liquefaction of the gas to prevent cavitation. After the desired operating temperature and pressure of the precipitating vessel were stabilized, the prepared lignin solution —— DMF was added to the weighed lignin particles and then the mixture

was sonicated for 30 min at room temperature — was sprayed into the precipitator at the desired flow rate via a nozzle (inside diameter: 254 μm). The precipitated particles were collected on the membrane filter paper (pore size: 0.45 μm, PTFE, Millipore, Italy) in the filter which was made of SUS316. After all of the solution was supplied, the products in the filter was washed by continuously pumping with only CO_2 for 30 min to remove any residual solvent entrapped in the precipitated lignin particles. After the washing step, the filter and the precipitator were depressurized, and the filter was separated from the apparatus. From the separated filter, the particles were taken out and weighed to measure the recovery yield. The conditions employed for the PCA process and their recovery yields are reported in Table 1. The percent recovery of the precipitated particles was calculated by the quantity of the collected particles on the filter paper (g) divided by the quantity of the initial raw lignin (g) multiplied by 100%.

Determination of Hansen solubility parameters, distance and RED number

The basic of Hansen solubility parameters (HSPs) approach is the assumption that total cohesive energy (E) of a pure compound is made up of the additive contributions from nonpolar (dispersion) interactions (E_d), polar (dipole-dipole and dipole-induced-dipole) interactions (E_p), and hydrogen bonding or other specific association interactions (including Lewis acid−base interactions (E_h):[57]

$$E = E_d + E_p + E_h \qquad (1)$$

Dividing each contribution by the molar volume,

$$\frac{E}{V} = \frac{E_d}{V} + \frac{E_p}{V} + \frac{E_h}{V} \qquad (2)$$

gives the square of the total solubility parameters as the sum of the squares of the Hansen dispersion (δ_d), polar (δ_p), and hydrogen bonding (δ_h) solubility parameters, so that

$$\delta_t^2 = \delta_d^2 + \delta_p^2 + \delta_h^2 \qquad (3)$$

where

$$\delta_d^2 = \frac{E_d}{V}; \quad \delta_p^2 = \frac{E_p}{V}; \quad \delta_h^2 = \frac{E_h}{V} \qquad (4)$$

The determination of HSPs for compounds that are gases at ambient conditions is usually based on room temperature solubility of the gas in a range of different liquids of known δ_d, δ_p, and δ_h. Those liquids that show the highest solubility for the gas are assumed to have HSPs closer to those of the gas than those liquids that have lower solubilities for the gas.

The solubility parameter values for CO_2 have been determined by Williams,[105] based on this suggested methodology, at 298.2 K as being δ_d, δ_p, and δ_h equal to 15.6, 5.2, and 5.8 MPa$^{1/2}$, respectively. From equation 3, the determined HSP values for CO_2 result in a total CO_2 solubility parameter of 17.4 MPa$^{1/2}$.

$$\begin{aligned}\delta_t^2 &= \delta_d^2 + \delta_p^2 + \delta_h^2 \\ &= (15.6)^2 + (5.2)^2 + (5.8)^2 = 304.04 \text{ MPa} \\ \delta_t &= 17.4 \text{ MPa}^{1/2}\end{aligned}$$

The pressure volume temperature (PVT) equations of state (EOS) that calculates the total (Hildebrand) CO_2 solubility parameter value was used to determine the combination of pressure and molar volume corresponding to T = 298.2 K and $\delta_t = [T (\partial P/\partial T)_v - P]^{1/2}$ = 17.4 MPa$^{1/2}$ that give:

$$\begin{aligned}P &= 91.7 \text{ MPa} \\ V_{CO2} &= 39.13 \text{ cm}^3/\text{mol} \qquad (5)\end{aligned}$$

In the case of DMF, the isothermal compressibility coefficients K_T and volumetric thermal expansion coefficient α were calculated at the designed experimental pressures and temperatures based on the reference data at 298.2 K and 0.1 MPa from Egorov and Kolker.[106] These data (K_T and α) were used to calculate the molar volume of DMF (V_{DMF}) at the specified temperature and pressure by using PVT EOS: $dV/V = \alpha \, dT - K_T \, dP$. On the other hand, the solubility parameters values for DMF from a reference[57] measured at 298.2 K and partial pressure of 0.1 MPa were δ_d, δ_p, δ_h and δ_t equal to 17.4, 13.7, 11.3 and 24.86 MPa$^{1/2}$, respectively.

Afterwards, HPS values for CO_2 and DMF at the designed experimental pressures and temperatures were calculated based on these reference set at HSP values, using derived pressure and temperature integral functions, as shown in the following equations (6-8):

$$\frac{\delta_{dref}}{\delta_d} = \left(\frac{V_{ref}}{V}\right)^{-1.25} \qquad (6)$$

$$\frac{\delta_{pref}}{\delta_p} = \left(\frac{V_{ref}}{V}\right)^{-0.5} \qquad (7)$$

$$\frac{\delta_{href}}{\delta_h} = \exp\left[-1.32 \times 10^{-3}(T_{ref} - T) - \ln\left(\frac{V_{ref}}{V}\right)^{0.5}\right] \qquad (8)$$

Furthermore, the solubility parameter distances (R_a) between two materials as a function of experimental temperatures and pressures were calculated based on their respective partial solubility parameter components using equation 9; where δ_{d1}, δ_{p1} and δ_{h1} are the centre point of the solute sphere; δ_{d2}, δ_{p2} and δ_{h2} are the solvent coordinates according to the centre point. In this case, the solubility parameters and radius of the sphere (R_0) for lignin were obtained from the reference;[107] δ_d, δ_p, δ_h and R_0 were 21.9, 14.1, 16.9 and 13.7 MPa$^{1/2}$, respectively.

$$(R_a)^2 = 4 (\delta_{d1} - \delta_{d2})^2 + (\delta_{p1} - \delta_{p2})^2 + (\delta_{h1} - \delta_{h2})^2 \qquad (9)$$

The physical affinity between lignin and the solvent (DMF)/antisolvent (CO_2) in the system were assessed by the ratio R_a/R_0 has been known as the RED number, reflecting the relative energy difference.

Characterization methods for raw and processed lignin particles

Morphology and particle size analysis. Field emission scanning electron microscopy (FESEM) and high resolution transmission electron microscopy (HRTEM) were used to examine the shape and size of raw and processed lignin particles. The FESEM images were acquired on a SURRA 55VP FE-SEM (Carl Zeiss, Germany) operated at 2 kV and various resolving powers after mounting lignin particles on aluminum specimen stubs and sputter coating with 10 nm platinum using a BAL-TEC/SCD 005 sputter coater (SoftComp, Germany). The HRTEM images were acquired on a JEM 3010 HR-TEM (JEOL, Japan) operated at an acceleration voltage of 300 kV with a GATAN Ultrascan CCD Camera after drop-casting the suspended samples in DI onto super-thin carbon film coated 300 mesh copper grids (Electron Microscopy Sciences, USA) and air drying the grids for overnight. Particle size distributions of the precipitated lignin were measured from the SEM images using ImageJ software.[108] The histogram of particle sizes obtained by SEM over 300 particles was fitted by a Gaussian function. A particle size analyzer Analysette 22 (MicroTech Plus, Fritsch, Germany) was used to measure particle size and size distribution of the raw lignin.

Porous structure analysis. The porosity parameters of the samples (*i.e.,* the nitrogen adsorption-desorption isotherms at 77.4 K, surface area, pore volume, and pore diameter) were determined using an ASAP 2020 (Accelerated Surface Area and Porosimetry) instrument (Micromeritics, USA). All samples were degassed at a temperature of 333.2 K for at least 4 h in a vacuum chamber prior to the sorption measurements. The total surface area, S_{BET}, was calculated by the multipoint BET (Brunauer-Emmett-Teller) method.[109] The mesopore surface area, S_{meso}, and micropore volume (pore size <2 nm), V_{mic}, were obtained from the *t*-plot method, based on the representation of the isotherm versus the thickness of the adsorbed layer on a non-porous reference material.[110] Total pore volume, V_{Tot}, was estimated from the amount adsorbed at relative pressure (P/P_0) = 0.98.[111] The pore diameters and pore size distributions were estimated by the BJH (Barrett-Joyner-Halenda) method from the desorption branches.

Attenuated total reflection-Fourier transform infrared (ATR-FTIR) spectroscopy. The chemical features of the samples were determined using a Nicolet 6700 FTIR spectrometer (Thermo Scientific, USA) equipped with a universal ATR accessory. ATR-FTIR spectra were obtained by averaging 32 scans from 4000 to 650 cm^{-1} at 4 cm^{-1} resolution for each background and sample spectrum, respectively. The ATR-FTIR spectra were baseline-corrected and normalized at the maximum of absorption at 1511-1512 cm^{-1} which is assigned to the aromatic skeleton stretch. The bands of absorption were identified. From these FTIR spectra, the condensation index (*CI*) was calculated for each lignin samples using equation (10):[79]

$$CI = \frac{\text{Sum of all minima between 1500 and 1050 cm}^{-1}}{\text{Sum of all maximum between 1600 and 1030 cm}^{-1}} \quad (10)$$

X-ray photoelectron spectroscopy. The chemical states of the component elements were examined using an AXIS-HSi XPS instrument (Shimadzu/Kratos, Ltd., Japan) equipped with an Mg Kα X-ray source operated at 150 W and a charge neutralizer. Spectra were recorded using an analyzer pass energy of 20 eV and a step size of 0.1 eV per step. The quantification was performed using the default relative sensitivity factor (RSF) values supplied by the XPS manufacturer. Data analysis was performed using CasaXPS software. Two point energy stable referencing was made using adventitious C (284.5 eV) and valance bond energy corrections. The percentages of individual elements detection were determined from the relative composition analysis of the peak areas of the bands.

X-ray diffraction. The crystal phases of the samples were investigated by a Rigaku Miniflex X-ray diffractometer (Tokyo, Japan) equipped with a Cu K$_{\alpha}$ radiation source (λ = 0.15406 nm) operated at 40 kV and 200 mA. Diffraction patterns were recorded using a 2ϑ range of 10−60° with a step size of 0.02°.

Thermal analysis. The glass transition temperature (T_g) determination of the samples was performed on a Q100 DSC (TA instrument, USA) using a N$_2$ flow rate of 50 mL/min. The samples of about 2−5 mg were sealed in aluminum pans and heated to 353.2 K at a rate of 278.2 K/min, and maintained for 30 min prior to being quenched to 273.2 K. The DSC thermograms were recorded by increasing the temperature to 473.2 K at a rate of 283.2 K/min. The thermal degradation (T_d) behavior of the samples was investigated using a Q500 TGA (TA Instrument, USA). Measurements were carried out under flowing N$_2$ of 60 mL/min at a heating rate of 283.2 K/ min over a temperature range of 308.2−1073.2 K, with an initial sample weight of approximately 2−5 mg.

UV-vis spectroscopy. The optical density, dispersion stability and pH stability of lignin nanoparticles in aqueous solutions were studied using an Evolution 201 UV-vis spectrophotometer (Thermo Scientific Inc., USA). The optical density was measured after suspending the lignin nanoparticles in DI (concentration: 0.1 g/L) and its absorption spectrum was recorded in the wavelength range of 240−600 nm. For dispersion stability studies, the percentages of UV transmittances at the wavelength 400 nm of the aqueous lignin suspensions in DI (concentration: 0.1 g/L) were determined within 30 min interval for 24 h in the UV−vis spectrophotometer. For pH stability studies, aqueous lignin suspensions were prepared with 50 mM phosphate buffer saline solution (pH: 7.4) and adjusted the pH vales (pH: 2−10) by using 1 M HCl or 1 M NaOH, and their spectra were recorded in the wavelength range of 240−600 nm. The same measurements were carried out for the raw lignin as a comparison.

Green Chemistry Accepted Manuscript

***In vitro* dissolution studies.** The *in vitro* dissolution studies were performed according to the United States Pharmacopeia (USP) paddle-stirring method using a DST-810 dissolution tester (LabFine, Korea).[112] 100 mg of lignin particles was added to 500 mL of DI water at 298.2 ± 273.4 K and agitated constantly at 100 rpm for 5 h. Sample of 3 mL was withdrawn at predetermined intervals, filtered through a 0.45 µm syringe filter (PVDF, Millipore Millex-HV, Merck, Japan) and replaced with 3 mL of DI water after each withdrawal. The absorbance of the filtrate was measured at a wavelength of 280 nm using an Evolution 201 UV-vis spectrophotometer (Thermo Scientific Inc., USA) and the soluble lignin concentration was calculated using the following equation:

$$C = A - A_0 / \varepsilon \times L \qquad (11)$$

where *C* is the lignin concentration (g/L), *A* is the absorption of sample, A_0 is the absorption of blank (DI water), ε is the absorption coefficient and *L* is the thickness of quartz cell (1 cm). Dissolution tests were performed in triplicate. The dissolution profiles were plotted on the basis of percentage of dissolved lignin verses incubation time.

Cytotoxicity assay

Microbial cell preparation. A derivative of *Pseudomonas aeruginosa*, PAO1, tagged with green fluorescent protein (GFP) which was kindly provided by Dr. M.J. Franklin (Montana State University, USA), was selected as the model bacterial strain. To obtain a single pure strain, we performed as described in our previous report.[113] Briefly, PAO1 was precultured on a tryptic soy agar (TSA, Difco, USA) plate supplemented with 100 mg/L of carbenicillin (Sigma-Aldrich, USA) overnight (18 h) at 310.2 K in an incubator (IB 25G, Lab Campanion, Korea). A fresh, single colony of PAO1 was inoculated in 10% tryptic soy broth (TBS, Difco, USA) and grown overnight on a shaker at 110 rpm and 310.2 K to reach a mid-exponential growth phase. Pure bacterial cells were harvested by centrifugation at 1000 g for 10 min. The supernatant was discarded and the remaining pellet was washed three times in 10 mM sterilized phosphate buffer saline (PBS, pH: 7.4) to remove nutrients. After washing, the cells were resuspended in PBS and the bacterial populations were estimated from the optical density of cells measured at a wavelength of 600 nm (OD_{600}) by a UV-vis Spectrophotometer (Agilent 8453, Agilent Technologies, USA). The initial concentrations of PAO1 GFP for viability and UV-vis assays were about 1×10^6 colony forming units (CFU) per mL.

Lignin solution preparation. 20 mg of lignin particles and 10 mL of 10 mM PBS were mixed and sonicated in a water bath Branson sonicator (Hatfield, PA) for 15 min at room temperature in order to thoroughly disperse the particles in the liquid. The suspended lignin solution was then diluted with 10 mM PBS to reach the total volume of 200 mL, and stirred for 30 min at 310.2 K to stabilize the mixture solution. The

concentration of the suspended lignin solution was 100 mg/L and used as the stock solution for viability and UV-vis assays.

Viability and UV-vis assays. The suspended lignin nanoparticles solution was mixed with PAO1 GFP suspension, initial concentration of 1×10^6 CFU/mL in deionized water, at a ratio of 10:1 and then incubated at 310.2 K with shaking at 120 rpm in a thermostatic orbital shaking incubator (WiseCube WIS-20, Daihan Scientific, Korea) for 3 d. Substrate blanks without bacteria and bacteria blanks without substrate were run in parallel. The aliquot of 1 mL was taken at predetermined time intervals, and immediately filtered with a 0.22 µm syringe filter (Toyo Roshi Kaisha Ltd., Japan). The absorbances of the soluble lignin contents were measured at 280 nm on an Evolution 201 UV-vis Spectrophotometer (Thermo Scientific, Inc., USA) to assess lignin degradation activity in PAO1 GFP. On the other hand, the concentration of PAO1 GFP in the samples were enumerated by the spread plate count method after incubating at predetermined time intervals. The images at 0 h and 24 h were visualized on a confocal laser scanning microscopy (CLSM 201, Eclipse 90i, EZ-C1, Nikon, Japan) and analyzed with a digital image analysis software, IMARIS (Bitplane AG, Switzerland). For CLSM images, 40 mL of solution was filtered with cellulose nitrate membrane (pore size: 0.22 µm, diameter: 47 mm, Advanced Microdevices Pvt. Ltd, India) and the samples on the membranes were stained with the Live/Dead bacterial viability kit (*Bac*Light, Molecular Probes, USA)[114] for 30 min. Live and dead cells were colored by green and red, respectively.

Conclusions

The highly mono-dispersed and uniform quasi-spherical lignin nanoparticles (mean particle diameter: 38 nm) were successfully synthesized by a facile, one pot green technology using the $clCO_2$ as an antisolvent. Besides, the lignin nanoparticles have relatively high specific surface area and porous structure which primarily composed of mesopores, and high purity as compared with the raw kraft lignin. The results clearly indicated that the surface of lignin nanoparticles were modified with high functional of hydroxyl, carbonyl and carboxyl groups which resulted in enhance solubility in water, high UV absorption and dispersion stability, more homogeneous thermal degradation and didn't show cytotoxicity with the studied bacteria: PAO1 GFP. It is apparently showed that the particle size, size distribution and aggregation/coalescing phenomena were strongly influenced on the operating conditions: density of the liquid CO_2 with respect to temperature and pressure, solution flow rate and initial solution concentration. This highlighted that the particle coalescences can be overcome by operating at relatively far above critical pressure of the MCP of the CO_2-DMF system (*i.e.,* 15.0 MPa). In particular, the PCA method is capable on industrial scale with environmentally friendly. Eventually, this study suggested that such biodegradable and biocompatible

lignin nanoparticles may find its applications as in cosmetics, health, and drug delivery system or other areas likes nanocomposite materials.

Acknowledgements

Notes and references

1   A. Mahapatro and D. K. Singh, *J. Nanobiotechnology*, 2011, **9**, 55−65.
2   T. Akagi, M. Baba and M. Akashi, *Adv. Polym. Sci.*, 2012, **247**, 31−64.
3   S. Saranya and K. V. Radha, *Polym. Plast. Technol. Eng.*, 2014, **53**, 1636−1646.
4   P. Musto, *Front. Chem.*, 2013, **1**, 1−4.
5   M. He, Y. Sun and B. Han, *Angew. Chem. Int. Ed.*, 2013, **52**, 9620−9633.
6   F. R. Wurm and C. K. Weiss, *Front. Chem.*, 2014, **2**, 1−13.
7   F. G. Calvo-Flores and J. A. Dobado, *ChemSusChem*, 2010, **3**, 1227−1235.
8   H. Hatakeyama and T. Hatakeyama, in Biopolymers, ed. B. A. Abe, K. Dušek and S. Kobayashi, Springer-Verlag, Berlin-Heidelberg, 2010, vol. 232, ch. 2, pp. 4−11.
9   J. H. Lora and W. G. Glasser, *J. Polym. Environ.*, 2002, **10**, 39−48.
10   T. Saito, R. H. Brown, M. A. Hunt, D. L. Pickel, J. M. Pickel, J. M. Messman, F. S. Baker, M. Keller and A. K. Naskar, *Green Chem.*, 2012, **14**, 3295−3303.
11   F. A. C. Faria, D. V. Evtuguin, A. Rudnitskaya, M. T. S. R. Gomes, J. A. B. P. Oliveria, M. P. F., Graça and L. C. Costa, *Polym. Int.*, 2012, **61**, 788−794.
12   E. Frank, L. M. Steudle, D. Ingildeev, J. M. Spörl and M. R. Buchmeiser, *Angew. Chem. Int. Ed.*, 2014, **53**, 2−39.
13   D.A. Baker and T. G. Rials, *J. Appl. Polym. Sci.*, 2013, **130**, 713−728.
14   V. K. Thakur and M. K. Thakur, *Int. J. Biol. Macromol.*, 2015, **72**, 834−847.
15   G. Gao, J. I. Dallmeyer and J. F. Kadla, *Biomacromolecules*, 2012, **13**, 3602−3610.
16   E. Ten, C. Ling, Y. Wang, A. Srivastava, L. A. Dempere and W. Vermerris, *Biomacromolecules*, 2014, **15**, 327−338.
17   D. Yiamsawas, G. Baier, E. Thines, K. Landfester and F. R. Wurm, *RCS Adv.*, 2014, **4**, 11661−11663.
18   C. Frangville, M. Rutkevicius, A. P. Richter, O. D. Velev, S. D. Stoyanov and V. N. Paunov, *ChemPhysChem*, 2012, **13**, 4235−4243.
19   Y. Qian, Y. Deng, X. Qiu, H. Li and D. Yang, *Green Chem.*, 2014, **16**, 2156−2163.
20   M. Tortora, F. Cavlieri, P. Mosesso, F. Ciaffardini, F. Melone and C. Crestini, *Biomacromolecules*, 2014, **15**, 1634−1643.
21   I-A. Gîlcă and V. I. Popa, *Cellulose Chem. Technol.*, 2013, **47**, 239−245.
22   Q. Lu, M. Zhu, Y. Zu, W. Liu, L. Yang, Y. Zhang, X. Zhao, X. Zhang, X. Zhang and W. Li, *Food Chem.*, 2012, **135**, 63−67.
23   T. Xu, N. Zhang, H. L. Nichols, D. Shi and X. Wen, *Mater. Sci. Eng. C*, 2007, **27**, 579−594.
24   A. Kumari, S. K. Yadav and S. C. Yadav, *Colloids Surf. B*, 2010, **75**, 1−18.
25   G. Cazacu, M. Capraru and V. I. Popa, in Advances in natural polymers composites and nanocomposites, ed. B. S. Thomas, P. M. Visakh and A. P. Mathew, Springer-Verlag, Berlin-Heidelberg, 2013, ch. 8, pp. 255−312.
26   K. Byrappa, S. Ohara and T. Adschiri, *Adv. Drug Deliv. Rev.*, 2008, **60**, 299−327.
27   F. Dehghani and N. R. Foster, *Curr. Opin. Solid State Mater. Sci.*, 2003, **7**, 363−369.
28   N. Foster, R. Mammucari, F. Dehghani, A. Barrett, K. Bezanehtak, E. Coen, G. Combes, L. Meure, A. Ng, H. L. Regtop and A. Tandya, *Ind. Eng. Chem. Res.*, 2003, **42**, 6476−6493.
29   A. Tabernero, E. M. M. del Valle and M. A. Galán, *Chem. Eng. Process.*, 2012, **60**, 9−25.
30   D. L. Tomasko, H. Li, D. Liu, X. Han, M. J. Wingert, L. J. Lee and K. W. Koelling, *Ind. Eng. Chem. Res.*, 2003, **42**, 6431−6456.
31   S. Mawson, S. Kanakia and K.P. Johnston, *J. Appl. Polym. Sci.*, 1997, **64,** 2105−2118.
32   S. D. Yeo and E. Kiran, *J. Supercrit. Fluids*, 2005, **34**, 287−308.
33   D. J. Dixon, G. Luna-Barcenas and K. P. Johnston, *Polymer*, 1994, **35**, 3998−4005.
34   L. Sze Tu, F. Dehghani and N. R. Foster, *Powder Technol.*, 2002, **126**, 134−149.
35   R. Bodmeier, H. Wang, D. J. Dixon, S. Mawson and K. P Johnston, *Pharm. Res.*, 1995, **12**, 1212−1217.
36   R. F. Falk and T. W. Randolph, *Pharm. Res.*, 1998, **15**, 1233−1237.
37   F. Fusaro, J. Kluge, M. Mazzotti and G. Muhrer, *J. Supercrit. Fluids*, 2009, **49**, 79−92.
38   D. J. Dixon, K. P. Johnston and R. A. Bodmeier, *AIChE J.*, 1993, **39**, 127−139.
39   C. Lin, K. M. Ng and C. Wibowo, *Ind. Eng. Chem. Res.*, 2007, **46**, 3580−3589.
40   K. Wu and J. Li, *J. Supercrit. Fluids*, 2008, **46**, 211−216.
41   Y. P´erez de Diego, H. C. Pellikaan, F. E. Wubbolts, G. J. Witkamp and P. J. Jansens, *J. Supercrit. Fluids*, 2005, **35**, 147−156.
42   E. Elizondo, A. Córdoba, S. Sala, N. Ventosa and J. Veciana, *J. Supercrit. Fluids*, 2010, **53**,108−114.
43   M. Sarkari, I. Darrat and B. L. Knutson, *AIChE J.*, 2000, **46**, 1850−1859.
44   C. S. Lengsfeld, J. P. Delplanque, V. H. Barocas and T. W. Randolph, *J. Phys. Chem. B*, 2000, **104**, 2725−2735.
45   B. Y. Shekunov, J. Baldyga and P. York, *Chem. Eng. Sci.*, 2001, **56**, 2421−2433.
46   Y. P´erez de Diego, F. E. Wubbolts and P. J. Jansens, *J. Supercrit. Fluids*, 2006, **37**, 53−62.
47   F. Miguel, A. Martín, F. Mattea and M. J. Cocero, *Chem. Eng. Process.*, 2008, **47**, 1594−1602.
48   I. De Marco and E. Reverchon, *Powder Technol.*, 2008, **183**, 239−246.
49   M. Rantakylä, M. Jäntti, O. Aaltonen and M. Hurme, *J. Supercrit. Fluids*, 2002, **24**, 251−263
50   M. A. Tavares-Cardoso, G. A. Monteiro, G. A. Cardoso, T. J. V. Prazeres, J. M. F. Figueiredo, J. M. G. Martinho, J. M. S. Cabral and A. M. F. Palavra, , *J. Supercrit. Fluids*, 2008, **44**, 238−244.
51   S.-C. Chang, M.-J. Lee and H-M Lin, *J. Supercrit. Fluids*, 2007, **40**, 420−432.
52   A. Tejado, C. Peňa, J. Labidi, J. M. Echevérria and I. Mondragon, *Bioresour. Technol.*, 2007, **98**, 1655−1663.
53   A. Vishtal and A. Kraslawski, *BioResources*, 2011, **6**, 3547−3568.

54   A. Zúñiga-Moreno and L. A. Galicia-Luna, *J. Chem. Eng. Data*, 2005, **50***, 1224-1233.

55   A. Erriguible, S. Laugier, M. Laté and P. Subra-Paternault, *J. Supercrit. Fluids*, 2013, **76**, 115–125.

56   I. Kikic, N. D. Zordi, M. Moneghini and D. Solinas, *J. Supercrit. Fluids*, 2010, **55**, 616–622.

57   C. M. Hansen, in Hansen solubility parameters: a user's handbook, 2nd edn., CRC press, Taylor & Francis Group, LLC, New York, 2007, ch. 1, pp. 1−26.

58   A. Kordikowski, A. P. Schenk, R. M. Van Nielen, and C. J. Peters, *J. Supercrit. Fluids*, 1995, **8**, 205−216.

59   D. To, R. Dave, X. Yin and S. Sundaresan, *AIChE J.*, 2009, **55**, 2807−2826.

60   N. Murillo-Cremaes, P. Subra-Paternault, J. Saurina, A. Roig and C. Domingo, *Colloid. Polym. Sci.*, 2014, **292**, 2475–2484.

61   M. A. Winters, B. L. Knutson, P. G. Debenedetti, H. G. Sparks and T. M. Przybycien, *J. Pharm. Sci.*, 1996, **85**, 586−594.

62   E. Reverchon, I. De Marco and E. Torino, *J. Supercrit. Fluids*, 2007, **43**, 126−138.

63   Y. Bakhbakhi, M. Asif, A. Chafidz and A. Ajbar, *Polym. Eng. Sci.*, 2013, **53**, 564-570.

64   I. De Marco and E. Reverchon, *J. Supercrit. Fluids*, 2011, **58**, 295–302.

65   S. Lowell, J. E. Shields, M. A. Thomas, and M. Thommes, in Characterization of porous solids and powders: surface area, pore size and density, ed. B. B. Scarlett, Kluwer Academic Publishers, The Netherlands, 2004, ch. 1, pp. 1−4.

66   F. Chen and J. Li, *Adv. Mater. Res.*, 2010, **113–114**, 1837−1840.

67   F. Chen, M. Xu, L. Wang and J. Li, *BioRes.*, 2011, **6**, 1262–1272.

68   L. I. Grishechko, G. Amaral-Labat, A. Szczurek, V. Fierro, B. N. Kuznetsov and A. Celzard, *Microporous Mesoporous Mater.*, 2013, **168**, 19−29.

69   L. I. Grishechko, G. Amaral-Labat, A. Szczurek, V. Fierro, B. N. Kuznetsov, A. Pizzi, and A. Celzard, *Ind. Crop. Prod.*, 2013, **41,** 347−355.

70   S. J. Gregg, *Colloids Surf.*, 1986, **21**, 109–124.

71   J. A. Dirksen and T. A. Ring, *Chem. Eng. Sci.*, 1991, **46**, 2389−2427.

72   P. H. Van Konynenburg and R. L. Scott, *Phil. Trans. R. Soc. Lond.*, 1980, **298**, 495–540.

73   A. J. Thote and R. B. Gupta, *Nanomed-Nanotechnol.*, 2005, **1**, 85–90.

74   A. Tenorio, M. D. Gordillo, C. Pereyra and E. J. Martínez de la Ossa, *J. Supercrit. Fluids*, 2007, **40**, 308–316.

75   G. D. Botsaris, in Industrial crystallization, ed. B. J. W. Mullin, Plenum, New York, 1976, pp. 3−22.

76   J. Estrin, in Preparation and properties of solid state materials, ed. B. W. R. Wilcox, Marcel Dekker, New York, 1976, vol. 2, pp. 1−42.

77   A. Tabernero, E. M. Martín del Valle and M. A. Galán, *Powder Technol.*, 2012, **217**, 177–188.

78   T. Fadli, A. Erriguible, S. Laugier and P. Subra-Paternault, *J. Supercrit. Fluids*, 2010, **52**, 193−202.

79   O. Faix, in Methods in lignin chemistry, ed. B. S. Y. Lin and C. W. Dence, Springer-Verlag, Berlin-Heilderberg, 1st edn., 1992, pp. 233−241.

80   C. G. Boeriu, D. Bravo, R. J. A. Gosselink and J. E. G. van Dam, *Ind. Crop. Prod.*, 2004, **20,** 205–218.

81   D. Schorra, P. N. Diouf and T. Stevanovic, *Ind. Crop. Prod.*, 2014, **52**, 65−73.

82   R. B. Santos, P. W. hart, H. Jameel and H.-M. Chang, *BioResources*, 2013, **8**, 1456-1477.

83   T. J. Fullerton, *J Wood Chem. Technol.*, 1987, **7**, 441−462.

84   C. G. Boeriu, D. Bravo1, R. J. A. Gosselink and J. E. G. van Dam, *Ind. Crops Prod.*, 2004, **20**, 205–218.

85   M. Malathi, R. Sabesan and S. Krishnan, *Current Sci.*, 2004, **86**, 838−842.

86   M. Ago, J. E. Jakes, L.-S. Johansson, S. Park, and O. J. Rojas, *ACS Appl. Mater. Interfaces*, 2012, **4**, 6849−6856.

87   G. E. Ledyashova and A. Z. Dorogochinskii, *UDC*, 1966, **3**, 33−35.

88   G. H. Ward and R. K. Schultz, *Pharm. Res.*, 1995, **12**, 773−779.

89   D. S. Argyropoulos, H. Sadeghifar, C. Cui, and S. Sen, *ACS Sustainable Chem. Eng.*, 2014, **2**, 264−271.

90   J. Bouajila, P. Dole, C. Joly and A. Limare, *J. Appl. Polym. Sci.*, 2006, **102**, 1445−1451.

91   G. Uçar, D. Meier, O. Faix and G. Wegener, *Eur. J. Wood Wood Prod.*, 2005, **63**, 57−63.

92   P. Gonugunta, S. Vivekanandhan, A. K. Mohanty and M. Misra, *World J. Nano Sci. Eng.*, 2012, **2**, 148−153.

93   S. Sahoo, M. Ö. Seydibeyoğlu, A. K. Mohanty and M. Misra, *Biomass Bioenerg.*, 2011, **35**, 4230−4237.

94   S. Chu, A. V. Subrahmanyam and G. W. Huber, *Green Chem.*, 2013, **15**, 125−136.

95   E. Jakab, O. Faix and F. Till, *J. Anal. Appl. Pyrolysis*, 1997, **40−41**, 171−186.

96   M. Brebu and C. Vasile, *Cellulose Chem. Technol.*, 2010, **44,** 353−363.

97   M. Wysokowski, L. Klapiszewski, D. Moszyński, P. Bartczak, T. Szatkowski, I. Majchrzak, K. Siwińska-Stefańska, V. V. Bazhenov and T. Jesionowski, *Mar. Drugs*, 2014, **12**, 2245−2268.

98   X. Ouyang, Y. Deng, Y. Quian, P. Zhang and X. Qiu, *Biomacromolecules*, 2011, **12**, 3313−3320.

99   K. Wang, F. Xu and R. Sun, *In. J. Mol. Sci.*, 2010, **11**, 2988−3001.

100   J. Teixeira, A. Gaspar, E. M. Garrido, J. Garrido and F. Borges, *BioMed. Res. Int.*, 2013, 2013, 1−11.

101   S. K. Das, C. Dickinson, F. Lafir, D. F. Brougham and E. Marsili, *Green Chem.*, 2012, **14**, 1322−1334.

102   H.-M. Ding and Y.-Q. Ma, *Sci. Rep.*, 2013, **3**, 1−6.

103   I. Sondi and B. Salopek-Sondi, *J. Colloid Interf. Sci.*, 2004, **275**, 177−182.

104   S. Sharifi, S. Behzadi, S. Laurent, M. L. Forrest, P. Stroeve and M. Mahmoudi, *Chem. Soc. Rev.*, 2012, **41**, 2323−2343.

105   L. Williams, Ph.D. Thesis, Colorado State University, Fort Collins, CO, 2001.

106   G. I. Egorov and A. M. Kolker, *Russ. J. Phys. Chem. A*, 2008, **82**, 2285−2291.

107   C. M. Hansen and A. Björkman, *Holzforschung*, 1998, **52**, 335−344.

108   G. Woehrle, J. Hutchison, S. Ozkar and R. Finke, *Image. Turk. J. Chem.*, 2006, **30**, 1−13.

109   S. Brunauer, P. H. Emmet and E. Teller, *J. Am. Chem. Soc.*, 1938, **60**, 309−319.

110   B. C. Lippens and J. H. de Boer, *J. Catal.*, 1965, **4**, 319−323.

111   K. S. W. Sing, D. H. Everett, R. A. W. Haul, L. Moscou, R. A. Pierotti, J. Rouquérol and T. Siemieniewska, *Pure Appl. Chem.*, 1985, **57**, 603−619.

112   J. L. Baxter, J. Kukura and F. J. Muzzio, *Int. J. Pharm.*, 2005, **292**, 17−28.

113   A. A. Myint, W. Lee, S. Mun, C. H. Ahn, S. Lee and J. Yoon, *Biofouling*, 2010, **26**, 313−321.

114   L. S. Boulos and M. H. N. Arsanious, *Heteroatom. Chem.*, 1999, **10**, 337−341.

A graphical abstract

A uniform, small quasi-spherical shape with relatively high BET surface area (nearly 92 m^2/g) of lignin nanoparticles were synthesized using a facile, one pot technology of compressed CO_2 antisolvent.